

Thin-Film Preparation and Characterization of $\text{Cs}_3\text{Sb}_2\text{I}_9$: A Lead-Free Layered Perovskite Semiconductor

Bayrammurad Saparov,^{†,‡} Feng Hong,^{§,||} Jon-Paul Sun,[⊥] Hsin-Sheng Duan,[†] Weiwei Meng,[§] Samuel Cameron,[⊥] Ian G. Hill,[⊥] Yanfa Yan,^{*,§} and David B. Mitzi^{*,†,‡}

[†]Department of Mechanical Engineering and Materials Science, Duke University, Box 90300 Hudson Hall, Durham, North Carolina 27708, United States

[‡]Department of Chemistry, Duke University, Durham, North Carolina 27708, United States

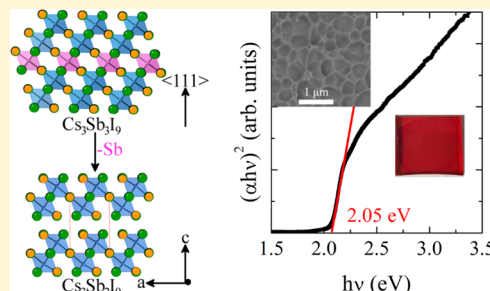
[§]Department of Physics and Astronomy and Center for Photovoltaics Innovation and Commercialization, The University of Toledo, Toledo, Ohio 43606, United States

^{||}Department of Physics, Shanghai University, Shanghai 200444, China

[⊥]Department of Physics and Atmospheric Science, Dalhousie University, Halifax, Nova Scotia B3H 3J5, Canada

S Supporting Information

ABSTRACT: Computational, thin-film deposition, and characterization approaches have been used to examine the ternary halide semiconductor $\text{Cs}_3\text{Sb}_2\text{I}_9$. $\text{Cs}_3\text{Sb}_2\text{I}_9$ has two known structural modifications, the 0-D dimer form (space group $P6_3/mmc$, no. 194) and the 2-D layered form ($P\bar{3}m1$, no. 164), which can be prepared via solution and solid-state or gas-phase reactions, respectively. Our computational investigations suggest that the layered form, which is a one-third Sb-deficient derivative of the ubiquitous perovskite structure, is a potential candidate for high-band gap photovoltaic (PV) applications. In this work, we describe details of a two-step deposition approach that enables the preparation of large grain ($>1\ \mu\text{m}$) and continuous thin films of the lead-free layered perovskite derivative $\text{Cs}_3\text{Sb}_2\text{I}_9$. Depending on the deposition conditions, films that are *c*-axis oriented or randomly oriented can be obtained. The fabricated thin films show enhanced stability under ambient air, compared to methylammonium lead(II) iodide perovskite films stored under similar conditions, and an optical band gap value of 2.05 eV. Photoelectron spectroscopy study yields an ionization energy of 5.6 eV, with the valence band maximum approximately 0.85 eV below the Fermi level, indicating near-intrinsic, weakly p-type character. Density functional theory (DFT) analysis points to a nearly direct band gap for this material (less than 0.02 eV difference between the direct and indirect band gaps) and a similar high-level of absorption compared to $\text{CH}_3\text{NH}_3\text{PbI}_3$. The photoluminescence peak intensity of $\text{Cs}_3\text{Sb}_2\text{I}_9$ is substantially suppressed compared to that of $\text{CH}_3\text{NH}_3\text{PbI}_3$, likely reflecting the presence of deep level defects that result in nonradiative recombination in the film, with computational results pointing to I_v , I_{Sb} , and V_1 as being likely candidates. A key further finding from this study is that, despite a distinctly layered structure, the electronic transport anisotropy is less pronounced due to the high ionicity of the I atoms and the strong antibonding interactions between the Sb *s* lone pair states and I *p* states, which leads to a moderately dispersive valence band.



INTRODUCTION

Methylammonium lead iodide ($\text{CH}_3\text{NH}_3\text{PbI}_3$) has emerged as a remarkable photovoltaic absorber material in recent years.^{1–3} Although devices incorporating $\text{CH}_3\text{NH}_3\text{PbI}_3$ as an absorber material demonstrate power conversion efficiencies (PCE) above 20%,⁴ fundamental issues remain, including the presence of the heavy-metal toxic element lead (Pb) and instability under ambient moist air. The efforts to address these issues mainly have focused on depositions of protective layers and altering the thin-film deposition procedure of the perovskite layer.^{5,6} A few materials solutions to the sensitivity and toxicity of $\text{CH}_3\text{NH}_3\text{PbI}_3$ have also been proposed.^{7,8} Homovalent substitution of lead with tin in $\text{CH}_3\text{NH}_3\text{SnI}_3$ addresses the issue of lead toxicity;⁷ however, the stability of the Sn-analogue is a concern because Sn normally prefers the tetravalent state,

and the divalent Sn-based materials are therefore prone to oxidation. Another proposed alternative is $(\text{PEA})_2(\text{CH}_3\text{NH}_3)_2\text{Pb}_3\text{I}_{10}$ (where PEA = phenylethylammonium),⁸ which is a layered derivative of the $\text{CH}_3\text{NH}_3\text{PbI}_3$ perovskite. This material demonstrates an open-circuit voltage of 1.18 V and a power conversion efficiency of 4.73%. More importantly, it is relatively stable in air containing 52% relative humidity for up to 46 days. The enhanced moisture stability of $(\text{PEA})_2(\text{CH}_3\text{NH}_3)_2\text{Pb}_3\text{I}_{10}$ is likely due to the presence of bulky organic PEA^+ cations. Because the fabricated films are highly oriented, with the perovskite layers parallel to the substrate, the

Received: May 26, 2015

Revised: July 7, 2015

Published: July 9, 2015

termination of the deposited film must occur with the hydrophobic organic layers protecting the anionic inorganic perovskite $[\text{Pb}_3\text{I}_{10}]^{4-}$ substructure. The anionic $[\text{Pb}_3\text{I}_{10}]^{4-}$ substructure is essentially identical to the $[\text{PbI}_3]^-$ network in the $\text{CH}_3\text{NH}_3\text{PbI}_3$ perovskite and, as such, should be similarly air/moisture-sensitive. Therefore, although some progress has been made, the search for alternative materials with enhanced stability and reduced toxicity must continue in order to bring halide perovskite-based absorbers to the market.

The perovskite structure offers remarkable tunability of the materials' dimensionality, the chemical content, crystal, and electronic structures.^{9,10} For example, tuning of the thickness of the inorganic perovskite layers from a single sheet ($n = 1$) to the parent 3D perovskite ($n = \infty$) in the $(\text{C}_4\text{H}_9\text{NH}_3)_2(\text{CH}_3\text{NH}_3)_{n-1}\text{Sn}_n\text{I}_{3n+1}$ series leads to a wide variation of physical properties, from a large band gap semiconductor for the former to more metallic-like character in the latter.¹¹ Taking advantage of this flexibility, large band gap semiconductors can be designed for colored and partially transparent PV. The significant interest in transparent and colored PV materials originates from the building-integrated photovoltaics (BIPV) concept, which advocates for a harmonious integration of PV materials that can cover the entire façade of a building.^{12–14} The above-mentioned $(\text{PEA})_2(\text{CH}_3\text{NH}_3)_2\text{Pb}_3\text{I}_{10}$, for example, was obtained as red crystals with a band gap of 2.06 eV.⁸ Such higher band gap perovskite derivatives are also candidates for use in tandem solar cells, which could overcome the Shockley–Queisser limit for single junction devices.¹⁵ Whereas the above family of $(\text{C}_4\text{H}_9\text{NH}_3)_2(\text{CH}_3\text{NH}_3)_{n-1}\text{Sn}_n\text{I}_{3n+1}$ or $(\text{PEA})_2(\text{CH}_3\text{NH}_3)_{n-1}\text{Pb}_n\text{I}_{3n+1}$ structures can be considered $\langle 100 \rangle$ -stacked perovskites, because they are composed of layers excised from the 3D perovskite by taking cuts from along the $\langle 100 \rangle$ crystallographic direction, another degree of flexibility involves the ability to select other layering schemes based on $\langle 110 \rangle$ and $\langle 111 \rangle$ cuts from the 3D structure. This flexibility is afforded by choice of the organic cation or the stoichiometry and size of atoms within a reaction mixture.^{10,16}

Here, we report a two-step deposition approach that enables the preparation of large grain ($>1\ \mu\text{m}$) and continuous thin films of the lead-free $\langle 111 \rangle$ -stacked layered perovskite derivative $\text{Cs}_3\text{Sb}_2\text{I}_9$. The layered modification of the purely inorganic $\text{Cs}_3\text{Sb}_2\text{I}_9$ has a band gap of 2.05 eV and shows enhanced air-stability compared to $\text{CH}_3\text{NH}_3\text{PbI}_3$. Depending on the deposition and heat treatment conditions, thin films that are preferentially or randomly oriented can be obtained. Photoelectron spectroscopy measurements indicate that the randomly oriented film is a near-intrinsic, weakly p-type material. Density functional theory (DFT) calculations performed on this compound show that it provides a nearly direct band gap (less than 0.02 eV difference between the direct and indirect band gaps) and similar high-level of absorption as exhibited by $\text{CH}_3\text{NH}_3\text{PbI}_3$. Relatively small effective masses are also obtained in the plane of the perovskite sheets and, surprisingly, the out-of-plane effective masses are also relatively small. The theoretical studies of defect properties suggest the presence of dominant deep level defects, in contrast to the generally shallow defect levels in $\text{CH}_3\text{NH}_3\text{PbI}_3$. Photoluminescence and initial PV device results are also presented and are consistent with a conclusion that defects will play a more critical role in the physics and prospective application of $\text{Cs}_3\text{Sb}_2\text{I}_9$ as an optoelectronic material.

■ EXPERIMENTAL SECTION

Materials. Several approaches were employed to grow films of $\text{Cs}_3\text{Sb}_2\text{I}_9$. In one approach, highly oriented (perovskite layers parallel to the substrate) $\text{Cs}_3\text{Sb}_2\text{I}_9$ thin films were fabricated through coevaporation of CsI and SbI_3 using Radak sources in an Angstrom Engineering evaporator. During coevaporation, the deposition rates, r , were kept close to $r(\text{CsI})/r(\text{SbI}_3) \approx 1.43$. The coevaporated films were annealed at temperatures between 250 and 350 °C in SbI_3 vapor under a quartz cover (within a N_2 -filled glovebox) to avoid SbI_3 loss from the film. In a second approach that yielded randomly oriented $\text{Cs}_3\text{Sb}_2\text{I}_9$ thin films, a CsI film was first deposited through evaporation and, subsequently, annealed in SbI_3 vapor. For both preferentially and randomly oriented $\text{Cs}_3\text{Sb}_2\text{I}_9$ film deposition approaches, the substrate was not intentionally heated and the base pressure preceding evaporation was $\sim 5 \times 10^{-7}$ Torr. The annealing time and temperature and the details of annealing procedure are important and these details of $\text{Cs}_3\text{Sb}_2\text{I}_9$ thin-film preparation are described in [Supporting Information](#).

Characterization Methods. FEI XL30 scanning electron microscopy (SEM) was used to obtain high resolution images of the fabricated thin films. Optical absorption measurements were carried out on a Shimadzu UV-3600 spectrophotometer. The optical absorption coefficients were extracted using Lambert's Law, $I = I_0 e^{-\alpha x}$, where I is the radiation intensity, α is the absorption coefficient, and x is the film thickness. Diffuse reflectance measurements were carried out using a QE-R quantum efficiency/reflectivity measurement system from Enlitech. Photoluminescence measurements were performed on a Horiba Jobi-Yvon LabRAM ARAMIS system using a 442 nm laser excitation. X-ray diffraction measurements were performed on a PANalytical Empyrean powder X-ray diffractometer. The X-ray diffraction experiments were carried out using Cu $K\alpha$ radiation and under ambient conditions. Crystal structure images were created using Crystal Maker software version 9.1.4. Air stability of the thin films was investigated by leaving them in a dark cabinet in ambient air, with a day-to-day relative humidity fluctuation ranging from 20 to 50%.

For photoelectron spectroscopy (PES), randomly oriented 200 and 300 nm thick $\text{Cs}_3\text{Sb}_2\text{I}_9$ films were prepared using the procedure described above and the samples were transferred into the chamber without air exposure. PES measurements, including ultraviolet photoelectron spectroscopy (UPS), inverse photoemission spectroscopy (IPES), and X-ray photoelectron spectroscopy (XPS), were conducted using as-loaded samples and after receiving different length sputtering treatments (i.e., Ar ion source with an extractor voltage of 3000 V and a beam current of 5 μA , rastered over a 10 mm \times 10 mm area). Reproducibility of spectra between the two film thicknesses was confirmed to ensure that sample charging was not an issue. For UPS and XPS studies, the analysis chamber was equipped with a hemispherical energy analyzer (Specs Phoibos 150). The UPS measurements were carried out using a He I ($h\nu = 21.22$ eV) source. A sample bias of -3 V was used to overcome the contact potential difference during measurement of the onset of photoemission (resulting UPS data are corrected for this bias). The XPS measurements were carried out using both Al $K\alpha$ (1486.6 eV) and Mg $K\alpha$ (1253.6 eV) sources. IPES measurements were performed in the isochromat mode using a homemade spectrometer located in the PES analysis chamber, with a resolution of approximately 0.6 eV as determined by the width of the Fermi edge of clean polycrystalline silver. The positions of the Fermi edge were used to align the UPS and IPES energy scales. Further details of characterization methods and preliminary device preparation attempts are provided in [Supporting Information](#).

Calculation Methods. The DFT calculations were performed using the projector-augmented wave (PAW) method,¹⁷ implemented in Vienna ab initio simulation package (VASP).¹⁸ The cutoff energy for the plane-wave basis set was 350 eV. The local-density approximations (LDA) of PAW, the generalized gradient approximation (GGA) of Perdew–Burke–Ernzerhof (PBE),¹⁹ and the screened hybrid Heyd–Scuseria–Ernzerhof (HSE)^{20,21} functionals

were used for exchange correlation. The HSE functional consists of 25% exact Hartree–Fock exchange mixed with 75% PBE exchange. All atoms were relaxed until the Hellmann–Feynman forces on them were smaller than 0.01 eV/Å. A $6 \times 6 \times 2$ and $6 \times 6 \times 1$ k -point mesh was used for layered and dimer structure, respectively. The GGA calculated lattice constants for layered and for dimer structure are $a = 8.661$ Å and $c = 10.625$ Å, and $a = 8.555$ Å and $c = 21.817$ Å, respectively. To study the defect properties, we have performed GGA calculations using a $(4 \times 4 \times 2)$ host supercell, with a focus on the Γ point. The optical properties are based on the calculation of the frequency-dependent dielectric function $\epsilon(\omega) = \epsilon_1(\omega) + i\epsilon_2(\omega)$,²² and the absorption coefficient $\alpha(\omega)$ can be described by $\alpha(\omega) = \omega / c(2(\epsilon_1^2(\omega) + \epsilon_2^2(\omega))^{1/2} - 2\epsilon_1(\omega))^{1/2}$, where $\epsilon_1(\omega)$ and $\epsilon_2(\omega)$ are the real part and the imaginary part of dielectric function, respectively.

RESULTS AND DISCUSSION

Structure Formation and Thin-Film Deposition. The crystal structure of the layered modification of $\text{Cs}_3\text{Sb}_2\text{I}_9$ ($P\bar{3}m1$, no. 164) is derived from the hypothetical perovskite compound CsSbI_3 (i.e., $\text{Cs}_3\text{Sb}_3\text{I}_9$) by removing every third Sb layer along $\langle 111 \rangle$ ($n = 2$) to achieve correct charge balance, as shown in Figure 1.¹⁰ The other known polymorph of $\text{Cs}_3\text{Sb}_2\text{I}_9$, the dimer

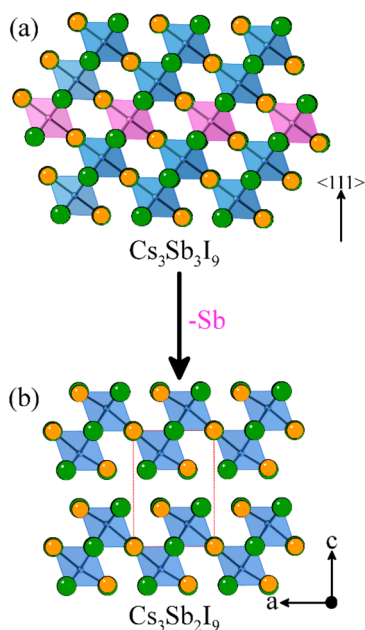


Figure 1. Removal of every third Sb layer along the $\langle 111 \rangle$ direction of (a) the perovskite structure results in (b) the 2D layered modification of $\text{Cs}_3\text{Sb}_2\text{I}_9$. Cs and I atoms are shown as orange and green spheres, respectively; Sb coordination polyhedra are shown in blue and pink.

modification (space group $P6_3/mmc$, no. 194), features SbI_6 octahedra fused into $\text{Sb}_2\text{I}_9^{3-}$ dimers through sharing of their triangular faces (see Supporting Information Figure S1).^{23–25} According to literature, the dimer form is synthesized from solution using a polar solvent, whereas the layered form is obtained from a solid state reaction at low temperatures.²³ The authors also argue that the two structural modifications can be transformed into each other through annealing. We attempted several synthesis strategies: bulk dimer $\text{Cs}_3\text{Sb}_2\text{I}_9$ formation from solution (see Supporting Information), deposition of a thin film of the dimer form by spin coating and, finally, annealing of the dimer form in order to obtain a thin film of the layered form of $\text{Cs}_3\text{Sb}_2\text{I}_9$. In agreement with the report, our reactions in acetonitrile and N,N -dimethylformamide (DMF) using a

stoichiometric mixture of reactants yielded bright-orange precipitate, which was confirmed to be the dimer form of $\text{Cs}_3\text{Sb}_2\text{I}_9$ using powder X-ray diffraction (PXRD). The subsequent annealing of the dimer form, however, did not yield the desired layered $\text{Cs}_3\text{Sb}_2\text{I}_9$ structure. Instead, with heating, evolution of CsI peaks in the XRD patterns was observed due to SbI_3 dissociation/evaporation from the material (see Supporting Information Figure S2).

To deposit the layered form as a thin film, then, we coevaporated CsI and SbI_3 onto our unheated substrates. The as-deposited red thin film contains amorphous regions and crystallites of $\text{Cs}_3\text{Sb}_2\text{I}_9$ (Figure 2a), which are oriented so that

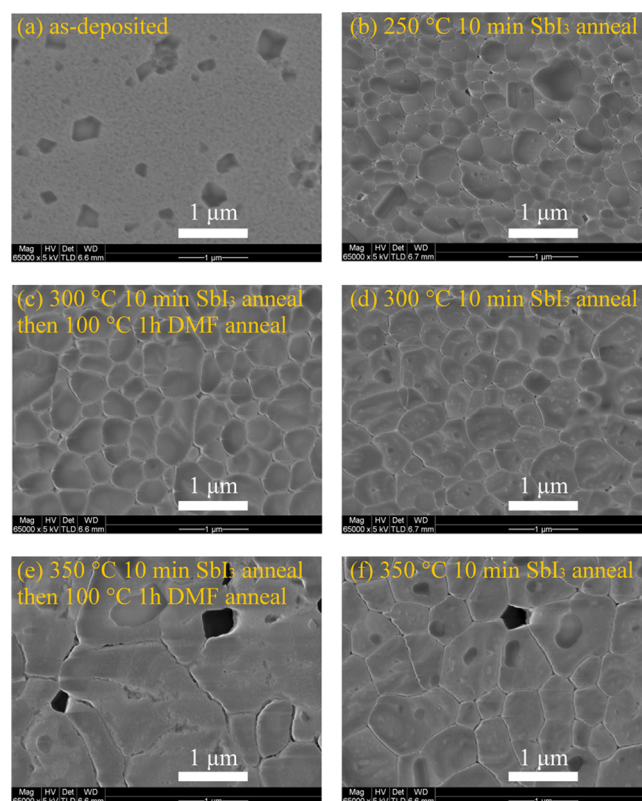


Figure 2. Scanning electron microscopy (SEM) images of (a) as-deposited and (b–f) annealed thin films of the layered $\text{Cs}_3\text{Sb}_2\text{I}_9$. (a) The initial film is deposited through coevaporation of CsI and SbI_3 , which is followed by annealing on a hot plate under a quartz cover inside a nitrogen-filled glovebox at (b) 250 °C, (d) 300 °C, or (f) 350 °C. Further DMF solvent annealing of (c) 300 °C-annealed and (e) 350 °C-annealed films at 100 °C gives smoother grain boundaries and larger grain sizes.

the layers (i.e., containing the ab plane) are parallel to the substrate surface, as evidenced by the fact that only $(00l)$ peaks are present in the PXRD patterns (Figure 3a). Upon annealing the as-deposited film in SbI_3 vapor, these small crystallites grow in a c -axis oriented fashion and the crystallinity of the film improves, yielding large-grained, highly oriented crystals (Figures 2, 3b). Increasing the annealing temperature also increases the SbI_3 evaporation rate. Consequently, if not handled with care, the resultant film may include a CsI impurity. We found that a short (1–2 s) dipping in acetone helps remove the CsI excess from the film; however, the resultant film is porous due to both vacant CsI pores and etching of the crystal grain boundaries. In the literature, there are reports of improved film quality and performances of lead

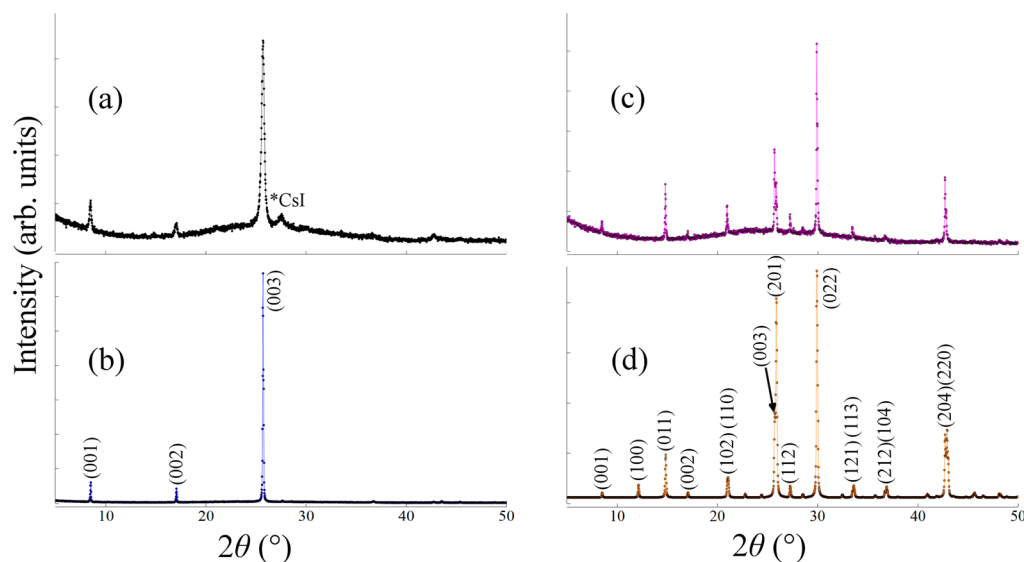


Figure 3. Powder X-ray diffraction patterns (Cu $K\alpha$ radiation) of layered $\text{Cs}_3\text{Sb}_2\text{I}_9$ films, which were subjected to various thermal treatment procedures: (a) An as-deposited film obtained from coevaporation of CsI and SbI_3 is largely amorphous or nanocrystalline and contains regions of unreacted binaries. (b) Annealing this coevaporated film in SbI_3 vapor at 300 °C for 10 min results in a highly oriented thin film. (c) A quicker reaction of CsI film with preheated SbI_3 vapor at 300 °C for 10 min results in a film that essentially preferred orientation. (d) The simulated pattern of the layered modification of $\text{Cs}_3\text{Sb}_2\text{I}_9$.

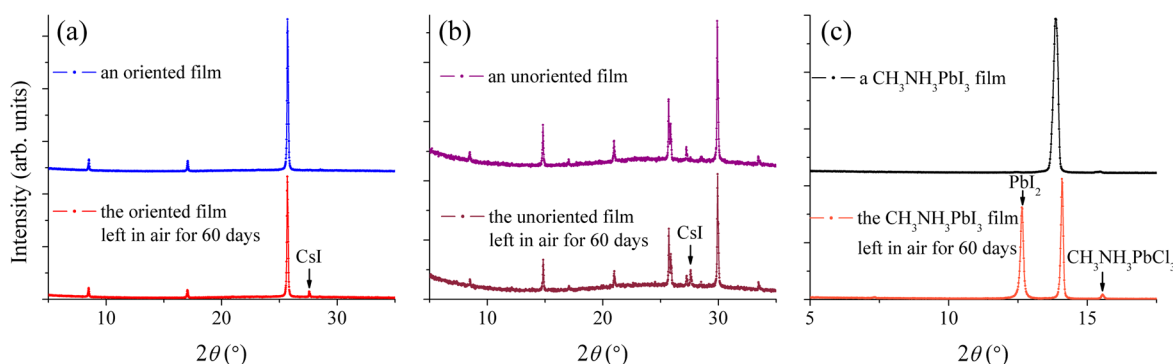


Figure 4. (a) Preferentially c -axis oriented and (b) unoriented (randomly oriented) films demonstrate a slow evolution of the CsI peaks for $\text{Cs}_3\text{Sb}_2\text{I}_9$ films left outside in ambient air for 60 days. In contrast, a faster degradation of (c) a $\text{CH}_3\text{NH}_3\text{PbI}_3$ film left in air is observed, with PbI_2 as a byproduct. See text and [Supporting Information](#) for details.

halide perovskite-based solar cell devices through solvent annealing²⁶ and, in agreement with this, we found that annealing in DMF vapor further increases the grain size (micrometer-sized grains are obtained, [Figure 2c,e](#)). Another important observation is that annealing at 350 °C under a quartz cover without excess SbI_3 vapor leads to a complete dissociation and evaporation of SbI_3 , leaving behind a white CsI film (confirmed through PXRD experiments). Upon cooling, the CsI film and trapped SbI_3 vapor react to form a film of the layered modification of $\text{Cs}_3\text{Sb}_2\text{I}_9$, which shows a much less oriented grain structure. The reconstructive phase transformation of the dimer form into the layered form reported by Yamada et al.²³ may not occur in the traditional sense of a phase transformation; rather, during annealing, the dimer form likely decomposes into CsI and SbI_3 vapor, which react upon subsequent cooling, thereby forming the layered modification.

After trying various conditions, annealing of the films at 300 °C for 10–30 min in SbI_3 vapor was determined to be the best approach for achieving large grain and continuous $\text{Cs}_3\text{Sb}_2\text{I}_9$ films. The films were subsequently cooled on top of the hot plate to 200 °C and then were quenched. The cooling step is

necessary to avoid the partial evaporation of SbI_3 from hot spots in the film, which can occur if the films are directly quenched from 300 °C. The choice of 200 °C as the quenching temperature also ensures that the surface of the $\text{Cs}_3\text{Sb}_2\text{I}_9$ film is not covered with a SbI_3 film. As demonstrated in [Figure 2](#), the largest grain sizes are obtained when the films are annealed at 350 °C; however, given the fact that there is an equilibrium between decomposition and formation of $\text{Cs}_3\text{Sb}_2\text{I}_9$ at this temperature, there is less control over the film quality and the resultant films are less reproducible compared to the 300 °C annealed films. The films in [Figure 2e,f](#) were obtained by heating the films at 350 °C in excess SbI_3 vapor with condensed droplets of SbI_3 on the quartz cover directly above the annealed films. This affords maintaining high SbI_3 vapor pressure²⁷ on the surface of the annealed films, which in turn discourages the decomposition of $\text{Cs}_3\text{Sb}_2\text{I}_9$, as monitored by the dark-red color of the film. If these conditions are not met, partial or complete discoloration of the film is immediately noticeable, signaling the decomposition of the $\text{Cs}_3\text{Sb}_2\text{I}_9$ film.

Following the first set of annealing experiments, we decided to do a sequential deposition of $\text{Cs}_3\text{Sb}_2\text{I}_9$, whereby CsI is

deposited through evaporation and the resulting CsI film is subsequently annealed in SbI_3 vapor. This was done first and foremost to gain better control over the orientation of the grains comprising the films because, due to the structural anisotropy of the layered material, a film configuration in which more of the grains orient with the *ab*-planes perpendicular to the substrate would likely be advantageous for PV device fabrication. To achieve this, we placed the CsI film (150 nm), which was obtained from thermal evaporation, together with SbI_3 powder simultaneously under a quartz cover (mimicking our first set of annealing experiments described above). Although this sequential deposition led to more randomly oriented crystals, the resultant film still showed a strong preferred orientation. A more completely randomized orientation of crystallites was finally achieved by annealing the CsI films in preheated SbI_3 vapor (Figure 3c). This was done by putting SbI_3 powder under the quartz cover at the desired annealing temperature and, after all of the SbI_3 is in the vapor phase and the temperature is stabilized, quickly placing the CsI films under the quartz cover. Under these conditions, there are many crystal formation centers within the CsI films and a quick reaction results in films that do not exhibit any substantial preferred orientation.

Air Stability. We monitored the air stability of thin films of the layered polymorph of $\text{Cs}_3\text{Sb}_2\text{I}_9$ for a prolonged period of time (up to 60 days) via X-ray diffraction measurements performed regularly (Figure 4). High temperature-annealed, well-crystallized thin films show only a very modest evolution of CsI impurity formation over the time scale of the experiment (Figure 4a,b). Interestingly, we do not find any significant difference in stabilities of *c*-axis oriented and randomly oriented films. To confirm that the impurity peak belongs to CsI, and not, for example, to the dimer form of $\text{Cs}_3\text{Sb}_2\text{I}_9$, several *c*-axis oriented thin films were scraped off of the substrate using a blade and, subsequently, X-ray diffraction measurements were performed on the powder (Supporting Information Figure S3). All peaks in the X-ray diffraction patterns were successfully ascribed to the layered $\text{Cs}_3\text{Sb}_2\text{I}_9$ and CsI. In comparison, under similar storing conditions, a $\text{CH}_3\text{NH}_3\text{PbI}_3$ thin film degrades more quickly, as indicated by a strong PbI_2 impurity peak after 60 days of ambient air exposure. We note that the stability of $\text{CH}_3\text{NH}_3\text{PbI}_3$ films depends on a variety of factors including the preparation method, storing conditions (humidity), and grain size and, depending on these factors, degradation can be noticeable in 4–5 days⁸ or not noticeable even after 28 days for the films cast onto mesoporous Al_2O_3 substrates.²⁸ The $\text{CH}_3\text{NH}_3\text{PbI}_3$ film used in this study showed clear signs of degradation after 2 weeks in air (Supporting Information Figure S4). Further discussion of the complex behavior of the $\text{CH}_3\text{NH}_3\text{PbI}_3$ thin film subjected to moist air is presented in the Supporting Information. In the recently reported layered lead halide perovskite $(\text{PEA})_2(\text{CH}_3\text{NH}_3)_2\text{Pb}_3\text{I}_{10}$, the enhanced moisture stability is attributed to the hydrophobic organic cation layer that protects the inorganic layered substructure.⁸ In contrast, the layered $\text{Cs}_3\text{Sb}_2\text{I}_9$ does not feature protective hydrophobic layers and its enhanced air stability must be due to its specific inorganic crystal structure or film grain structure.

Optical Properties. Annealing studies gave us a convenient way to control the crystallinity, grain size, and the orientation of the $\text{Cs}_3\text{Sb}_2\text{I}_9$ crystallites within a deposited film. The layered modification of $\text{Cs}_3\text{Sb}_2\text{I}_9$ is red as opposed to the orange color of the dimer modification, pointing to a lower band gap of the layered form. We carried out optical absorption measurements

using UV–vis spectroscopy for a high quality layered $\text{Cs}_3\text{Sb}_2\text{I}_9$ thin film. The calculated band gap from the Tauc plot of the absorbance data (Figure 5a) was found to be 2.05 eV, assuming

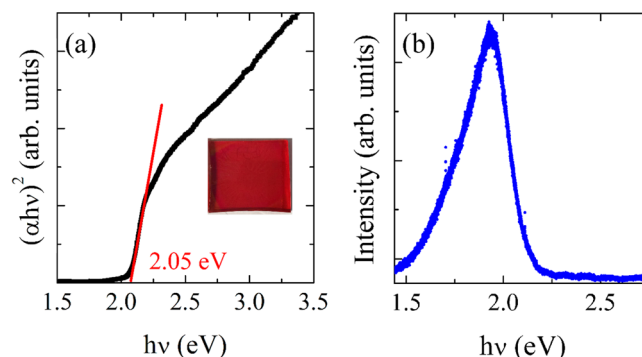


Figure 5. (a) Band gap of the layered modification of $\text{Cs}_3\text{Sb}_2\text{I}_9$ (inset shows a thin film) was calculated to be 2.05 eV from absorbance data using the Tauc relation. (b) A photoluminescence spectrum of $\text{Cs}_3\text{Sb}_2\text{I}_9$ obtained using 442 nm laser excitation. The $\text{Cs}_3\text{Sb}_2\text{I}_9$ film (as for $\text{CH}_3\text{NH}_3\text{PbI}_3$ analogues) shows signs of decomposition under the 442 nm HeCd laser, which is visible under a microscope (Supporting Information Figure S5); therefore, lower exposure time and laser power parameters are necessary for a reliable measurement (see Supporting Information).

a direct band gap. In comparison, the plot of $(\alpha h\nu)^{1/2}$ vs $h\nu$, assuming an indirect gap, yields a similar 2.00 eV band gap. The energy dependence of the absorption coefficient is provided in Supporting Information Figure S6. Upon leaving a $\text{Cs}_3\text{Sb}_2\text{I}_9$ film in ambient air for ~6 months, a 1.96 eV band gap is obtained from UV–vis spectroscopy, showing only minor impact of prolonged air exposure (Supporting Information Figure S7). Diffuse reflectance measurement was also performed on a bulk powder sample of layered $\text{Cs}_3\text{Sb}_2\text{I}_9$ obtained from solid-state reactions (see Supporting Information for details). Assuming a direct band gap and using the Kubelka–Munk model, a slightly lower band gap value of 1.95 eV is obtained for the powder sample (Supporting Information Figure S8).

In addition to UV–vis absorption, photoluminescence (PL) measurements on the thin-film samples give a broad peak with a maximum at ~633 nm (Figure 5b), which corresponds to 1.96 eV, consistent with the band gap values obtained from UV–vis spectroscopy and diffuse reflectance. More importantly, the intensity of the PL peak is noticeably lower compared to that of the $\text{CH}_3\text{NH}_3\text{PbI}_3$ perovskite film (see Supporting Information Figure S5).

Electronic Structure Calculations. To gain better insight into the electronic, optical, and defect properties of $\text{Cs}_3\text{Sb}_2\text{I}_9$, we performed DFT band structure calculations. The calculated HSE band structures for the layered and dimer phases are shown in Figure 6. The layered structure has a nearly direct band gap due to the very small difference between the direct and indirect band gap (less than 20 meV). The HSE calculated band gap is 2.06 eV, in good agreement with the experimental value of 2.05 eV (see above). However, a larger indirect band gap of 2.40 eV was found for the dimer structure, consistent with the lighter coloration for crystals of this phase. The partial density of states (PDOS) plots (see Figure 7) show that for both phases the upper valence band is composed of mixed I *p* and Sb lone-pair *s* states, whereas the lower conduction band is mainly derived from Sb *p* states.

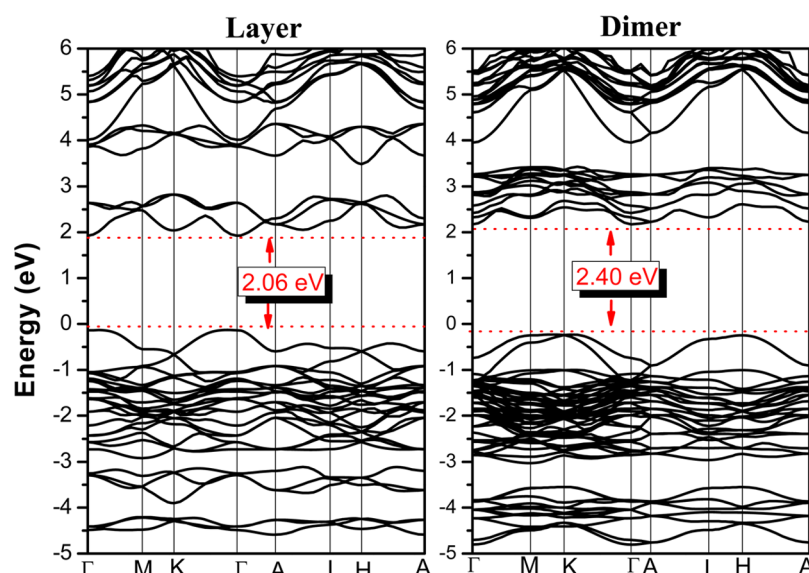


Figure 6. HSE calculated band structures of $\text{Cs}_3\text{Sb}_2\text{I}_9$ in layered and dimer modifications.

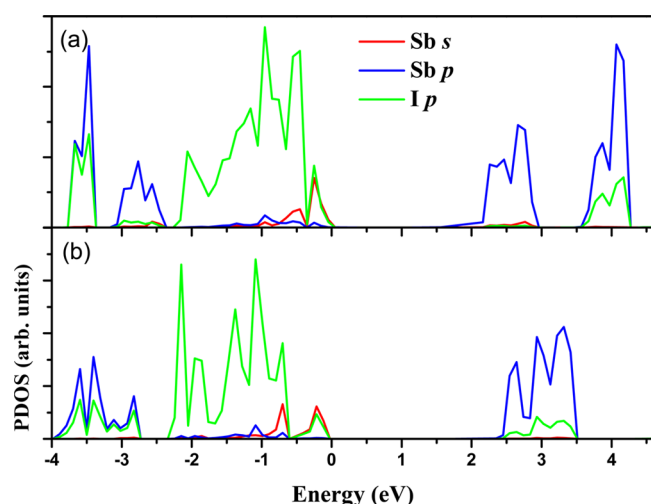


Figure 7. Partial density of states (PDOS) plots of the (a) layered and (b) dimer modifications of $\text{Cs}_3\text{Sb}_2\text{I}_9$.

The optical absorption coefficients for $\text{Cs}_3\text{Sb}_2\text{I}_9$ with both layered and dimer structures have been calculated based on the electronic structures (see Figure 8). For comparison, the calculated optical absorption coefficient for the organic–inorganic perovskite $\text{CH}_3\text{NH}_3\text{PbI}_3$ is also given. The absorption coefficients of both layered and dimer structures are as high as that of $\text{CH}_3\text{NH}_3\text{PbI}_3$. Meanwhile, an onset energy of about 2.0 eV for the layered structure was found and the dimer structure has a much higher onset energy (around 2.5 eV) due to its larger indirect band gap. Such high absorption coefficients for the $\text{Cs}_3\text{Sb}_2\text{I}_9$ phases can be understood by their electronic structures. Because the valence bands are comprised of $\text{I } p + \text{Sb } s$ orbitals and the conduction bands are derived from $\text{Sb } p$ orbitals, the optical transitions are expected to be from $(\text{I } p + \text{Sb } s)$ to $\text{Sb } p$. The p -orbital character of both the valence and conduction bands leads to a high joint density of states and therefore an unusually large optical absorption coefficient, as for $\text{CH}_3\text{NH}_3\text{PbI}_3$.²⁹ In $\text{CH}_3\text{NH}_3\text{PbI}_3$, the optical transitions are from $(\text{I } p + \text{Pb } s)$ to $\text{Pb } p$, and because the substitution of divalent Pb with trivalent Sb involves a metal cation with a

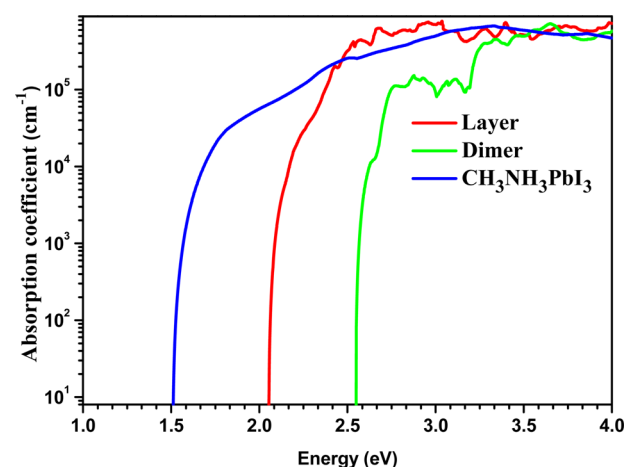


Figure 8. Calculated absorption coefficients for $\text{Cs}_3\text{Sb}_2\text{I}_9$ with the layered and dimer structures as compared to that of $\text{CH}_3\text{NH}_3\text{PbI}_3$.

similar electronic configuration,²⁹ the compositions of frontier orbitals are also similar in $\text{CH}_3\text{NH}_3\text{PbI}_3$ and $\text{Cs}_3\text{Sb}_2\text{I}_9$ phases.

Between the two polymorphs of $\text{Cs}_3\text{Sb}_2\text{I}_9$, the layered modification appears to be the more promising form for photovoltaic applications. Although not generally considered ideal for the absorber layer, the 0-D nature of the dimer form of $\text{Cs}_3\text{Sb}_2\text{I}_9$ does not necessarily disqualify the material from use in a solar cell device. To illustrate this point, another metal deficient perovskite derivative, Cs_2SnI_6 (half of the Sn sites are vacant in the 3D perovskite framework), featuring isolated SnI_6^{2-} octahedra, has recently been used as a hole transport material.³⁰ Interestingly, for a compound featuring isolated octahedra, the valence and conduction bands are remarkably dispersive in Cs_2SnI_6 , similar to the dimer modification of $\text{Cs}_3\text{Sb}_2\text{I}_9$, suggesting that the effective masses of charge carriers could be relatively small for these compounds comprised of 0-D metal halide units. Unlike Cs_2SnI_6 , which has a direct band gap of ~ 1.3 eV, however, the fact that the 0-D dimer modification of $\text{Cs}_3\text{Sb}_2\text{I}_9$ has a large indirect band gap of 2.4 eV makes it less promising compared to the 2D layered form, which exhibits a nearly direct 2.06 eV band gap. Therefore, we focus our

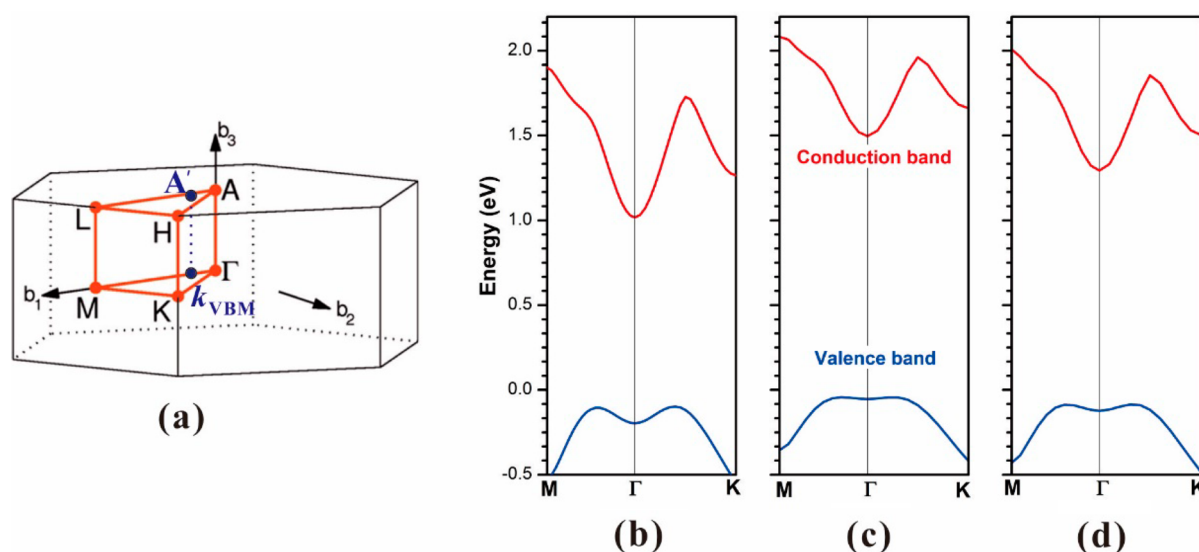


Figure 9. (a) Brillouin zone of a hexagonal lattice, and (b–d) the top of valence band and bottom of conduction band along M-Γ-K with LDA, PBE, and PBE using experimental lattice constant calculations, respectively, for layered $\text{Cs}_3\text{Sb}_2\text{I}_9$.

attention on the more promising 2D layered polymorph of $\text{Cs}_3\text{Sb}_2\text{I}_9$ in this study.

The valence and conduction bands are dispersive for the layered structure, indicating that electron and hole masses (m_e^* , m_h^*) should not be very large. It should be pointed out that the layered structure has only a nearly direct band gap, i.e., the valence band maximum (VBM) is not located exactly at the Γ -point. We have calculated the band structures using various exchange functionals and lattice constants and found that the difference between the direct and indirect band gaps is very small, i.e., less than 0.02 eV. The slight energy difference between the direct and indirect band gaps does not affect optical absorption, but it does affect the calculation of hole effective mass because the VBM is not exactly at the Γ -point. The k_{VBM} we used to calculate m_h^* is shown in Figure 9a. Furthermore, we found that the dispersion of the top of the valence band depends on the lattice constants. The lattice constants and band gaps calculated using different functionals are tabulated in Table 1. For comparison, the results of PBE

experimental lattice constants result in medium band dispersions. Consequently, the calculated effective masses, shown in Table 2, also depend on the lattice constants (although the different modeling approaches all yield qualitatively similar results).

Table 2. Calculated Effective Masses (m^*) with Different Theoretical Treatment for the $\text{Cs}_3\text{Sb}_2\text{I}_9$ Layered Structure

calculation method	m^*			
	hole		electron	
	$k_{[001]}$	$k_{[100]}$	$k_{[001]}$	$k_{[100]}$
PAW (LDA) (fully relaxed)	0.84	0.42	0.51	0.34
PBE (fully relaxed)	0.88	0.70	0.66	0.54
PBE (experimental lattice)	0.91	0.62	0.56	0.46
HSE (experimental lattice)	0.68	0.60	0.62	0.44

Table 1. Calculated Hexagonal Lattice Parameters (a , c) and Band Gaps (E_g) for the Layered Modification of $\text{Cs}_3\text{Sb}_2\text{I}_9$

	PAW (LDA)	PBE (GGA)	HSE	experimental
a (Å)	8.159	8.661	8.639	8.420 ²³
c (Å)	10.109	10.625	10.618	10.386 ²³
E_g (eV)	1.12	1.55	2.06	1.38 (1.89) ^a

^aPBE (HSE) calculated band gap using experimental lattice constants.

and HSE calculations with experimental lattice constants are also given. Our results suggest that PBE and HSE calculations overestimate the lattice constants, whereas the LDA calculation underestimates it. Generally, smaller lattice constants indicate stronger cation–anion bonding, resulting in more dispersive bands. To show clearly the difference of band dispersions calculated using LDA and PBE, the top of the valence band and bottom of the conduction band are given in Figure 9b–d. The LDA calculations (Figure 9b) give the most dispersive bands due to the smallest lattice constant, whereas the PBE calculations give the most flat valence band (Figure 9c) due to the largest lattice parameters. The PBE calculations using the

The effective masses along the $k_{[001]}$ are larger than those along the $k_{[100]}$, in accordance with the structural anisotropy in the layered material. Therefore, to produce a film with better transport properties, a film with perovskite layers perpendicular to the substrate is preferred. It should be pointed out, however, that for a layered structure, the hole effective mass along the $k_{[001]}$ is not very large. This is due to the fact that the valence band is rather dispersive (see Figure 6), which is attributed to the high ionicity of the I atoms and the strong antibonding interactions between the Sb s lone pair states and I p states. This observation is important and it indicates that, in some cases, the layered nature of a material may not be a large detriment for PV application.

In addition to effective masses, defects play an important role in determining the electronic properties of semiconductors. To investigate the defect properties of $\text{Cs}_3\text{Sb}_2\text{I}_9$, we have considered the intrinsic point defects, including acceptor-like defects such as cation vacancies (V_{Cs} , V_{Sb}), iodine interstitial (I_i), Cs on Sb cation substitution (Cs_{Sb}), anion on cation antisite substitution (I_{Cs} , I_{Sb}), and donor-like defects such as iodine vacancy (V_{I}), cation interstitial (Cs_i , Sb_i), Sb on Cs substitution (Sb_{Cs}), and cation on anion antisite substitution (Cs_i , Sb_i). Because of a lower structural symmetry, the atomic

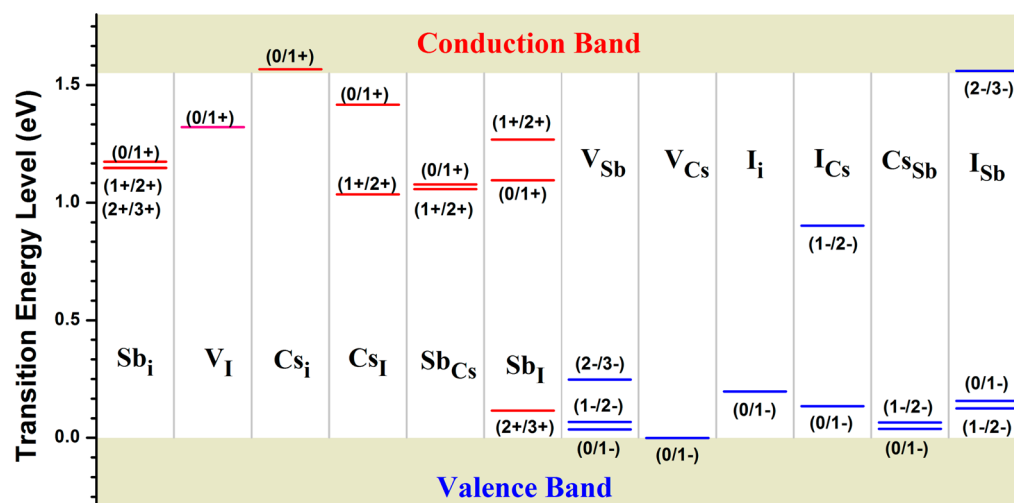


Figure 10. Calculated transition energy levels of intrinsic donors (red lines) and acceptors (blue lines) in $\text{Cs}_3\text{Sb}_2\text{I}_9$.

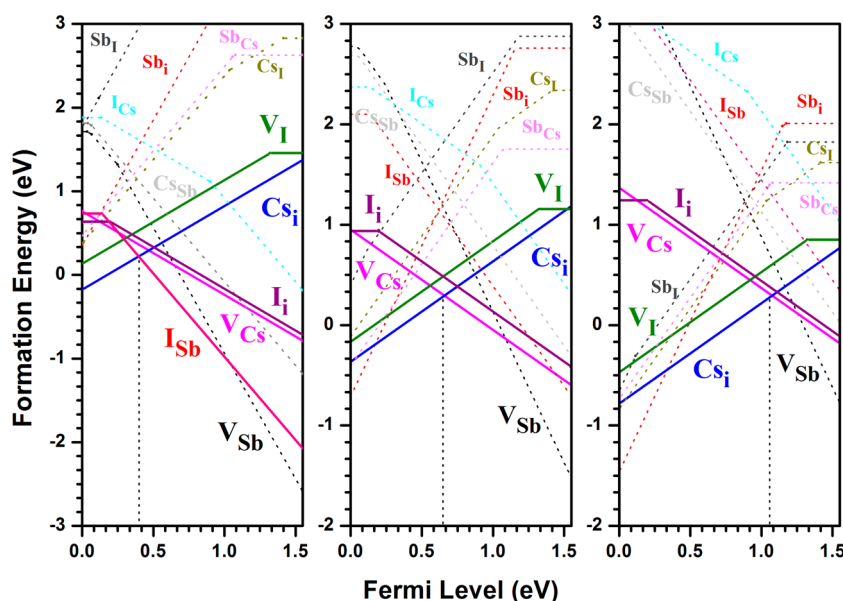


Figure 11. GGA calculated formation energies of intrinsic point defects in $\text{Cs}_3\text{Sb}_2\text{I}_9$ with layered structure and chemical potentials at A (I-rich/Sb-poor), B (moderate), and C (I-poor/Sb-rich). The vertical dotted lines indicate the Fermi level pinning. See text for descriptions of chemical potentials at A, B, and C. For the GGA calculation, the band gap was determined to be 1.55 eV (Table 1).

structures of defects in $\text{Cs}_3\text{Sb}_2\text{I}_9$ are more complex than similar defects in $\text{CH}_3\text{NH}_3\text{PbI}_3$. We have tested all the structures and have considered the configuration with the lowest energy for each defect. For example, there are two types of sites for Cs (1a and 2d) and I (3e and 6i), and therefore, there are two types of V_{Cs} and V_{I} . Our results suggest that the V_{Cs} and V_{I} with the lower energies and more stable configurations are at Cs 1a and I 6i sites, respectively. It was also found that Sb_{i} , as expected, favors the interlayer site, whereas Cs_{i} prefers an intralayer site (see Supporting Information Figure S9 for defect structures).

In general, defects that produce deep levels in the bandgap act as nonradiative recombination centers and are detrimental to solar cell performance. We used the standard method for the calculation of transition energy levels and formation energies for defects.^{31–33} The calculated transition energy levels for the above-considered defects in $\text{Cs}_3\text{Sb}_2\text{I}_9$ are shown in Figure 10. It is seen that only V_{Cs} and Cs_{i} are shallow acceptors and donors, respectively. All other defects create deep levels in the bandgap

of $\text{Cs}_3\text{Sb}_2\text{I}_9$. We note that although $\text{Cs}_3\text{Sb}_2\text{I}_9$ is a perovskite derivative, the defect properties are quite different from that in the $\text{CH}_3\text{NH}_3\text{PbI}_3$ perovskite. The difference can be understood from the qualitative model for predicting the levels of defects in crystals.³⁴ For example, most donor defects produce deeper levels in $\text{Cs}_3\text{Sb}_2\text{I}_9$ than in $\text{CH}_3\text{NH}_3\text{PbI}_3$. This is largely due to the fact that the Sb *p* atomic orbitals are more localized than the Pb *p* atomic orbitals. Consequently, the Sb *p*–I *p* antibonding is stronger than the Pb *p*–I *p* antibonding, which in turn implies the energy difference between the anion's *p* orbital and the conduction band minimum (CBM) is larger for $\text{Cs}_3\text{Sb}_2\text{I}_9$ than for $\text{CH}_3\text{NH}_3\text{PbI}_3$. As a result the donor defects exhibit deeper levels in $\text{Cs}_3\text{Sb}_2\text{I}_9$ than in $\text{CH}_3\text{NH}_3\text{PbI}_3$. Additionally, the weaker *s*–*p* antibonding coupling seen in $\text{Cs}_3\text{Sb}_2\text{I}_9$ is partially responsible for the slightly deeper acceptor levels.

Figure 11 shows the calculated defect formation energies as a function of Fermi level position under three different growth

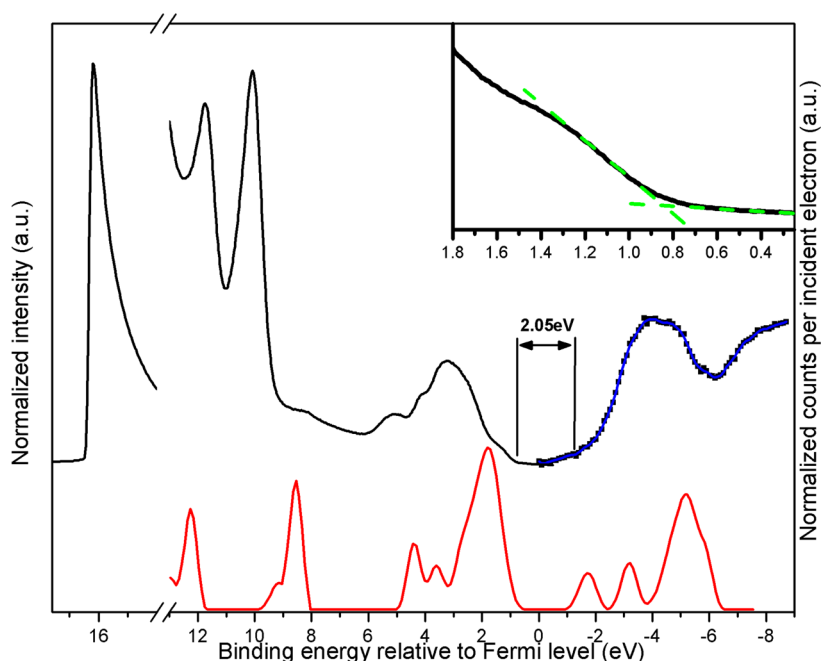


Figure 12. Combined UPS (He I)/IPES spectra (black) showing the onset of photoemission in the valence and conduction band regions of the 30 s sputtered 300 nm $\text{Cs}_3\text{Sb}_2\text{I}_9$ film. Below, a density of states (DOS) plot (red) is provided for comparison. The DOS plot represents the results from the computational study (discussed in the previous section), convolved with a 0.5 eV full width at half-max (fwhm) Gaussian and converted to a binding energy scale relative to the Fermi level. The smooth blue line through IPES data points is intended as a guide to the eye. Because of the slowly varying IPES background, the conduction band edge cannot be uniquely determined. The expected band gap measured from the valence band edge (determined from the UPS data) is drawn for comparison. The inset shows a close-up view of the valence band maximum with green tangent lines used to determine the edge location.

conditions, A (I-rich/Sb-poor, $\mu_{\text{Cs}} = -3.07$ eV, $\mu_{\text{Sb}} = -1.815$ eV, $\mu_{\text{I}} = 0$ eV), B (moderate, $\mu_{\text{Cs}} = -2.88$ eV, $\mu_{\text{Sb}} = -0.75$ eV, $\mu_{\text{I}} = -0.30$ eV), and C (I-poor/Sb-rich, $\mu_{\text{Cs}} = -2.465$ eV, $\mu_{\text{Sb}} = 0$ eV, $\mu_{\text{I}} = -0.605$ eV). At chemical potential point A, i.e., I-rich/Sb-poor, the dominant defects are I_{v} , V_{Cs} , and I_{Sb} . Under this growth condition, $\text{Cs}_3\text{Sb}_2\text{I}_9$ should exhibit moderate *p*-type conductivity, as the Fermi level is pinned at 0.38 eV above the VBM by I_{Sb} and Cs_{i} . At chemical potential point B, i.e., moderate, the dominant defects are I_{v} , V_{Cs} , Cs_{v} , and V_{I} . While I_{i} and V_{Cs} are acceptors, V_{I} and Cs_{i} are donors. In this case, the Fermi level is pinned at 0.66 eV above the VBM by V_{Cs} and Cs_{v} , and therefore $\text{Cs}_3\text{Sb}_2\text{I}_9$ should be either intrinsic or slightly *p*-type. Note that this Fermi level position (i.e., near intrinsic to slightly *p*-type) is approximately what has been observed in the present films using UPS, as described later. At chemical point C, i.e., I-poor/Sb-rich, the dominant defects are Cs_{i} and V_{I} . $\text{Cs}_3\text{Sb}_2\text{I}_9$ grown under this condition should be a moderate *n*-type semiconductor, as the Fermi level is pinned at 1.07 eV above the VBM by V_{Cs} and Cs_{v} .

Overall, our electronic band structure and optical properties calculations for $\text{Cs}_3\text{Sb}_2\text{I}_9$ suggest that this material exhibits promising optical properties, comparable to that of $\text{CH}_3\text{NH}_3\text{PbI}_3$; however, the defect properties of $\text{Cs}_3\text{Sb}_2\text{I}_9$ are distinctly different from that of $\text{CH}_3\text{NH}_3\text{PbI}_3$. In $\text{Cs}_3\text{Sb}_2\text{I}_9$, the dominant defects are V_{Cs} , I_{v} , I_{Sb} , Cs_{v} , and V_{I} , and among these, only Cs_{i} and V_{Cs} produce shallow levels, whereas I_{v} , I_{Sb} , and V_{I} produce deep levels. In addition to the slightly indirect nature of the band gap, the deep level defects could partially contribute to the suppressed PL peak intensity observed for the layered $\text{Cs}_3\text{Sb}_2\text{I}_9$ thin films. In contrast, all dominant defects produce only shallow levels in $\text{CH}_3\text{NH}_3\text{PbI}_3$.³⁵ Therefore, to use $\text{Cs}_3\text{Sb}_2\text{I}_9$ as a photovoltaic material or for other optoelectronic

applications, it is expected that careful control of defects and/or defect passivation will be necessary.

X-ray Photoelectron Spectroscopy (XPS)/Ultraviolet Photoelectron Spectroscopy (UPS)/Inverse Photoemission Spectroscopy (IPES). To probe the electronic structure experimentally, photoelectron spectroscopy (PES) measurements were conducted. Randomly oriented films prepared for PES measurements were analyzed as-loaded and after receiving 30 s, 5 min, or 10 min of sputtering. The as-loaded samples showed negligible carbon contribution to the XPS spectra; however, small amounts of oxygen are evident next to the Sb $3d_{5/2}$ peak (Supporting Information Figure S10). After 30 s of sputtering, however, this oxygen contribution severely diminishes (Supporting Information Figure S11). The change to the UPS spectra with 30 s of sputtering involves a reduction in the density of states in the 9–4 eV binding energy region. Despite these changes, the figures of merit deduced from the UPS spectra (emission onset and valence band maximum) remain unchanged. Longer sputtering times resulted in a shift of UPS and XPS features, and the appearance of another Sb peak in the XPS spectra at approximately 1.6 eV lower binding energy. We attribute these changes to the loss of SbI_3 from the films under longer sputtering times, in agreement with the sample decomposition observed during PL measurements. Note that the sample surface composition deduced for the as-loaded sample from XPS is consistent with the expected bulk composition, and the XPS data after sputtering confirms that long sputtering treatments lead to loss of both Sb and I (see Supporting Information Table S1). Therefore, the samples sputtered for 30 s were deemed to be the best representation of the bulk $\text{Cs}_3\text{Sb}_2\text{I}_9$ material.

From the UPS spectra (Figure 12), the ionization energy is calculated to be 5.6 eV, with the valence band maximum approximately 0.85 eV below the Fermi level. In conjunction with the measured optical gap of 2.05 eV, this implies $\text{Cs}_3\text{Sb}_2\text{I}_9$ is a near-intrinsic, weakly p-type material. The IPES spectrum displays a slowly varying background leading up to the conduction band edge. This makes an absolute determination of the location of the edge difficult to determine; however, a bandgap of 2.05 eV is consistent with the combined UPS and IPES spectra. The combined UPS/IPES spectra is also in a good agreement with the calculated DOS for the layered $\text{Cs}_3\text{Sb}_2\text{I}_9$.

Photovoltaic Device Results. From the results of UPS and IPES, a glass/FTO/c-TiO₂/Cs₃Sb₂I₉/PTAA/Au architecture was chosen as appropriate for device fabrication attempts (see Supporting Information Figure S12 for energy band alignment diagram). Our initial attempts to incorporate Cs₃Sb₂I₉ into a PV device using this architecture yielded open-circuit voltages of $V_{oc} = 250\text{--}300$ meV, with however overall device performance remaining low (<1%) (see Supporting Information, Figure S13). While these early low-performance results likely reflect the issues discussed above related to deep defects (and resulting recombination), they are also likely impacted by the very early stage of optimization of the device structure.

CONCLUSIONS

In summary, we can reproducibly create high quality thin films of the lead-free layered perovskite derivative $\text{Cs}_3\text{Sb}_2\text{I}_9$, which exhibits a 2.05 eV band gap and enhanced stability in ambient air compared to analogous $\text{CH}_3\text{NH}_3\text{PbI}_3$ films. In addition to the structural relationship with the hybrid organic–inorganic lead halide perovskites, simple electron counting shows another important advantage of this material: the trivalent Sb^{3+} in $(\text{Cs}^+)_3(\text{Sb}^{3+})_2(\text{I}^-)_9$ possesses a similar electronic configuration to the divalent Pb^{2+} in $(\text{CH}_3\text{NH}_3^+)(\text{Pb}^{2+})(\text{I}^-)_3$. Generally, the considered Pb-free alternatives to $\text{CH}_3\text{NH}_3\text{PbI}_3$ have featured homovalent substitution of divalent Pb with Sn. This work highlights that the heterovalent substitution of Pb and Sn with trivalent pnictogens could be another promising alternative. Because these substitutions are isoelectronic, advantageous features of the electronic band structures such as the presence of metal lone pair *s* orbitals in the valence band and (halide *p* + metal *s*) to (metal *p*) optical transitions are expected to be preserved.

In methylammonium lead iodide, the advantageous defect physics and small hole effective mass are attributed to the antibonding coupling of the Pb *s*- and I *p*-orbitals,³⁵ which are only partly applicable in $\text{Cs}_3\text{Sb}_2\text{I}_9$. The layered $\text{Cs}_3\text{Sb}_2\text{I}_9$ exhibits small hole effective masses both along and, surprisingly, perpendicular to the anionic $[\text{Sb}_2\text{I}_9]^{3-}$ layers; however, the I_I , I_Sb , and V_I defects produce deep levels. Both preferentially and randomly oriented thin films suffer from the presence of harmful defects, which act as centers of nonradiative recombination, thereby suppressing photoluminescence intensity. Further fine-tuning of band gap, doping, and especially defect concentrations will be required to enable fabrication of higher efficiency and improved stability lead-free solar cell devices based on the $\text{Cs}_3\text{Sb}_2\text{I}_9$ absorber. Importantly, this work paves the way to other Sb (and Bi) based perovskites for photovoltaic and related optoelectronic applications, including those based on other cuts from the 3-D framework.^{36,37}

ASSOCIATED CONTENT

Supporting Information

Details of bulk syntheses, thin-film deposition, and postannealing treatments, as well as characterization methods and device fabrication. The Supporting Information is available free of charge on the ACS Publications website at DOI: 10.1021/acs.chemmater.5b01989.

AUTHOR INFORMATION

Corresponding Authors

*For D.B.M.: E-mail, david.mitzi@duke.edu.

*For Y.Y.: E-mail, yanfa.yan@utoledo.edu.

Notes

The authors declare no competing financial interest.

ACKNOWLEDGMENTS

The information, data, or work presented herein was funded in part by the Office of Energy Efficiency and Renewable Energy (EERE), U.S. Department of Energy, under award number DE-EE0006712. One of the authors (B.S.) acknowledges support from a Department of Energy (DOE) Office of Energy Efficiency and Renewable Energy (EERE) Postdoctoral Research Award administered by the Oak Ridge Institute for Science and Education (ORISE) for the DOE. ORISE is managed by Oak Ridge Associated Universities (ORAU) under DOE contract number DE-AC05-06OR23100. All opinions expressed in this paper are the authors' and do not necessarily reflect the policies and views of DOE, ORAU, or ORISE. See the Supporting Information section of this article for more information.

REFERENCES

- (1) Kojima, A.; Teshima, K.; Shirai, Y.; Miyasaka, T. Organometal Halide Perovskites as Visible-Light Sensitizers for Photovoltaic Cells. *J. Am. Chem. Soc.* **2009**, *131*, 6050–6051.
- (2) Burschka, J.; Pellet, N.; Moon, S. J.; Humphry-Baker, R.; Gao, P.; Nazeeruddin, M. K.; Gratzel, M. Sequential deposition as a route to high-performance perovskite-sensitized solar cells. *Nature* **2013**, *499*, 316–319.
- (3) Green, M. A.; Ho-Baillie, A.; Snaith, H. J. The emergence of perovskite solar cells. *Nat. Photonics* **2014**, *8*, 506–514.
- (4) *Research Cell Efficiency Records*; National Center for Photovoltaics at the National Renewable Energy Laboratory: Golden, CO; www.nrel.gov/ncpv/ (accessed May 13, 2015).
- (5) Habisreutinger, S. N.; Leijtens, T.; Eperon, G. E.; Stranks, S. D.; Nicholas, R. J.; Snaith, H. J. Carbon Nanotube/Polymer Composites as a Highly Stable Hole Collection Layer in Perovskite Solar Cells. *Nano Lett.* **2014**, *14*, 5561–5568.
- (6) Mei, A. Y.; Li, X.; Liu, L. F.; Ku, Z. L.; Liu, T. F.; Rong, Y. G.; Xu, M.; Hu, M.; Chen, J. Z.; Yang, Y.; Gratzel, M.; Han, H. W. A hole-conductor-free, fully printable mesoscopic perovskite solar cell with high stability. *Science* **2014**, *345*, 295–298.
- (7) Hao, F.; Stoumpos, C. C.; Cao, D. H.; Chang, R. P. H.; Kanatzidis, M. G. Lead-free solid-state organic-inorganic halide perovskite solar cells. *Nat. Photonics* **2014**, *8*, 489–494.
- (8) Smith, I. C.; Hoke, E. T.; Solis-Ibarra, D.; McGehee, M. D.; Karunadasa, H. I. A Layered Hybrid Perovskite Solar-Cell Absorber with Enhanced Moisture Stability. *Angew. Chem., Int. Ed.* **2014**, *53*, 11232–11235.
- (9) Mitzi, D. B., Synthesis, Structure, and Properties of Organic-Inorganic Perovskites and Related Materials. In *Progress in Inorganic Chemistry*; John Wiley & Sons, Inc.: New York, 2007; pp 1–121.
- (10) Mitzi, D. B. Templating and structural engineering in organic-inorganic perovskites. *J. Chem. Soc., Dalton Trans.* **2001**, 1–12.

- (11) Mitzi, D. B.; Feild, C. A.; Harrison, W. T. A.; Guloy, A. M. Conducting tin halides with a layered organic-based perovskite structure. *Nature* **1994**, *369*, 467–469.
- (12) Lee, K.-T.; Fukuda, M.; Joglekar, S.; Guo, L. J. Colored, see-through perovskite solar cells employing an optical cavity. *J. Mater. Chem. C* **2015**, *3*, 5377–5382.
- (13) Eperon, G. E.; Burlakov, V. M.; Goriely, A.; Snaith, H. J. Neutral Color Semitransparent Microstructured Perovskite Solar Cells. *ACS Nano* **2014**, *8*, 591–598.
- (14) Zhang, W.; Anaya, M.; Lozano, G.; Calvo, M. E.; Johnston, M. B.; Míguez, H.; Snaith, H. J. Highly Efficient Perovskite Solar Cells with Tunable Structural Color. *Nano Lett.* **2015**, *15*, 1698–1702.
- (15) Beiley, Z. M.; McGehee, M. D. Modeling low cost hybrid tandem photovoltaics with the potential for efficiencies exceeding 20%. *Energy Environ. Sci.* **2012**, *5*, 9173–9179.
- (16) Mitzi, D. B.; Wang, S.; Feild, C. A.; Chess, C. A.; Guloy, A. M. Conducting Layered Organic-inorganic Halides Containing <110>-Oriented Perovskite Sheets. *Science* **1995**, *267*, 1473–1476.
- (17) Blochl, P. E. Projector augmented-wave method. *Phys. Rev. B: Condens. Matter Mater. Phys.* **1994**, *50*, 17953–17979.
- (18) Kresse, G.; Furthmüller, J. Efficient iterative schemes for ab initio total-energy calculations using a plane-wave basis set. *Phys. Rev. B: Condens. Matter Mater. Phys.* **1996**, *54*, 11169–11186.
- (19) Perdew, J. P.; Burke, K.; Ernzerhof, M. Generalized gradient approximation made simple. *Phys. Rev. Lett.* **1996**, *77*, 3865–3868.
- (20) Heyd, J.; Scuseria, G. E.; Ernzerhof, M. Hybrid functionals based on a screened Coulomb potential. *J. Chem. Phys.* **2003**, *118*, 8207–8215.
- (21) Paier, J.; Hirschl, R.; Marsman, M.; Kresse, G. The Perdew-Burke-Ernzerhof exchange-correlation functional applied to the G2–1 test set using a plane-wave basis set. *J. Chem. Phys.* **2005**, *122*, 234102.
- (22) Gajdoš, M.; Hummer, K.; Kresse, G.; Furthmüller, J.; Bechstedt, F. Linear optical properties in the projector-augmented wave methodology. *Phys. Rev. B: Condens. Matter Mater. Phys.* **2006**, *73*, 045112.
- (23) Yamada, K.; Sera, H.; Sawada, S.; Tada, H.; Okuda, T.; Tanaka, H. Reconstructive Phase Transformation and Kinetics of Cs₃Sb₂I₉ by Means of Rietveld Analysis of X-Ray Diffraction and ¹²⁷I NQR. *J. Solid State Chem.* **1997**, *134*, 319–325.
- (24) Chabot, B.; Parthe, E. Cs₃Sb₂I₉ and Cs₃Bi₂I₉ with the hexagonal Cs₃Cr₂Cl₉ structure type. *Acta Crystallogr., Sect. B: Struct. Crystallogr. Cryst. Chem.* **1978**, *34*, 645–648.
- (25) Ivanov, Y. N.; Sukhovskii, A. A.; Lisin, V. V.; Aleksandrova, I. P. Phase Transitions of Cs₃Sb₂I₉, Cs₃Bi₂I₉, and Cs₃Bi₂Br₉ Crystals. *Inorg. Mater.* **2001**, *37*, 623–627.
- (26) Xiao, Z.; Dong, Q.; Bi, C.; Shao, Y.; Yuan, Y.; Huang, J. Solvent Annealing of Perovskite-Induced Crystal Growth for Photovoltaic-Device Efficiency Enhancement. *Adv. Mater.* **2014**, *26*, 6503–6509.
- (27) Sime, R. J. The vapor pressures and bond energies of some antimony halides. *J. Phys. Chem.* **1963**, *67*, 501–503.
- (28) Christians, J. A.; Miranda Herrera, P. A.; Kamat, P. V. Transformation of the Excited State and Photovoltaic Efficiency of CH₃NH₃PbI₃ Perovskite upon Controlled Exposure to Humidified Air. *J. Am. Chem. Soc.* **2015**, *137*, 1530–1538.
- (29) Yin, W.-J.; Shi, T.; Yan, Y. Unique Properties of Halide Perovskites as Possible Origins of the Superior Solar Cell Performance. *Adv. Mater.* **2014**, *26*, 4653–4658.
- (30) Lee, B.; Stoumpos, C. C.; Zhou, N. J.; Hao, F.; Malliakas, C.; Yeh, C. Y.; Marks, T. J.; Kanatzidis, M. G.; Chang, R. P. H. Air-Stable Molecular Semiconducting Iodosalts for Solar Cell Applications: Cs₂SnI₆ as a Hole Conductor. *J. Am. Chem. Soc.* **2014**, *136*, 15379–15385.
- (31) Wei, S. H. Overcoming the doping bottleneck in semiconductors. *Comput. Mater. Sci.* **2004**, *30*, 337–348.
- (32) Yan, Y.; Wei, S. H. Doping asymmetry in wide-bandgap semiconductors: Origins and solutions. *Phys. Status Solidi B* **2008**, *245*, 641–652.
- (33) Freysoldt, C.; Grabowski, B.; Hickel, T.; Neugebauer, J.; Kresse, G.; Janotti, A.; Van de Walle, C. G. First-principles calculations for point defects in solids. *Rev. Mod. Phys.* **2014**, *86*, 253.
- (34) Yin, W.-J.; Shi, T.; Yan, Y. Superior Photovoltaic Properties of Lead Halide Perovskites: Insights from First-Principles Theory. *J. Phys. Chem. C* **2015**, *119*, 5253–5264.
- (35) Yin, W.-J.; Shi, T.; Yan, Y. Unusual defect physics in CH₃NH₃PbI₃ perovskite solar cell absorber. *Appl. Phys. Lett.* **2014**, *104*, 063903.
- (36) Mitzi, D. B.; Brock, P. Structure and Optical Properties of Several Organic–Inorganic Hybrids Containing Corner-Sharing Chains of Bismuth Iodide Octahedra. *Inorg. Chem.* **2001**, *40*, 2096–2104.
- (37) Mitzi, D. B. Organic–Inorganic Perovskites Containing Trivalent Metal Halide Layers: The Templating Influence of the Organic Cation Layer. *Inorg. Chem.* **2000**, *39*, 6107–6113.